nature neuroscience

Functional organization and population dynamics in the mouse primary auditory cortex

Gideon Rothschild[1,2], Israel Nelken[1,2] & Adi Mizrahi[1,2]

Cortical processing of auditory stimuli involves large populations of neurons with distinct individual response profiles. However, the functional organization and dynamics of local populations in the auditory cortex have remained largely unknown. Using *in vivo* two-photon calcium imaging, we examined the response profiles and network dynamics of layer 2/3 neurons in the primary auditory cortex (A1) of mice in response to pure tones. We found that local populations in A1 were highly heterogeneous in the large-scale tonotopic organization. Despite the spatial heterogeneity, the tendency of neurons to respond together (measured as noise correlation) was high on average. This functional organization and high levels of noise correlations are consistent with the existence of partially overlapping cortical subnetworks. Our findings may account for apparent discrepancies between ordered large-scale organization and local heterogeneity.

Cortical processing of sensory information is carried out by large networks of neurons. In these networks, it is generally accepted that the spatial location of each neuron defines its broad functional properties, whereas the coordinated neuronal activity has important implications for information processing and eventually for behavior[1–3]. Thus, measuring the activity of populations of neurons whose precise locations are known is fundamental to understanding how neuronal populations code sensory information.

In the auditory cortex, electrophysiological recordings have revealed the response properties of neurons to sound frequency and intensity and other sound features[4–6]. Large-scale imaging techniques and multi-unit recordings have characterized the global organization of the auditory cortex, revealing its division into separate fields and the gross organization in them[4,7,8]. Although large-scale imaging and recording techniques often produce smooth maps of response characteristics such as tonotopy, single-unit recordings indicate that response profiles may vary considerably, even for closely located neurons[6,9]. Thus, the issue of the local homogeneity (or lack thereof) in the auditory cortex remains unclear.

Recently, *in vivo* two-photon calcium imaging has proven to be well-suited for studying the functional micro-architecture of neural populations in the cortex. Studies in the visual[10,11] and barrel cortices[12,13] have started to unravel the local organization in these regions. We applied this method to study both the micro-architecture and the local network dynamics of the primary auditory cortex (A1). How similar or variable are the response properties of neighboring neurons in A1? Are there any obvious organizational principles in local populations? And to what extent are the responses of individual neurons in the network independent or correlated?

To answer these questions, we imaged neural population activity in mouse A1. We imaged the responses to pure tones of dozens of neurons simultaneously and up to 114 well-isolated neurons from each mouse. By deriving the response properties of individual neurons in small cortical patches, we found that local populations in A1 were highly heterogeneous. Analysis of simultaneous responses indicated that the average pair-wise noise correlations in local populations were high. Our results highlight the transition from smooth global maps to local heterogeneity in A1. We suggest a model of partially overlapping subnetworks to account for this functional architecture.

RESULTS

In vivo two-photon calcium imaging in A1

To characterize the functional architecture and dynamics of local networks in A1, we performed *in vivo* two-photon calcium imaging in anesthetized, freely breathing mice (**Fig. 1**). We loaded cells in the auditory cortex with a mixture of Fluo-4 a.m. and SR101 using the multicell bolus loading technique[14]. Fluo-4 stained neurons, astrocytes and neuropil in a spherical volume with a diameter of ~250 µm. SR101 selectively stained astrocytes and diffused more readily throughout A1. Loading was optimal ~40 min post injection, at which time hundreds of neurons could be detected at depths of up to 450 µm, corresponding to cortical layers 2/3 (**Fig. 1a**, **Supplementary Movie 1** and **Supplementary Fig. 1**). To maximize the data acquisition speed, we used line scans through neuronal somata (**Fig. 1a**,**b**). We imaged sequentially from up to ten different depths in each mouse, which enabled us to image the activity of hundreds of cells in a single injection site. To verify that the imaging was performed in A1, we labeled neurons in the same stereotactic coordinates using electroporation of dextran-rhodamine. Consistent with A1-thalamic connectivity[15], rhodamine-labeled terminals and retrogradely stained cell bodies were always visible in the ventral division of the medial geniculate body ($n = 6$ mice; **Fig. 1e**).

[1]Department of Neurobiology, Institute of Life Sciences and [2]The Interdisciplinary Center for Neural Computation, The Hebrew University of Jerusalem, Jerusalem, Israel. Correspondence should be addressed to A.M. (mizrahia@cc.huji.ac.il).

Received 7 October 2009; accepted 4 December 2009; published online 31 January 2010; doi:10.1038/nn.2484

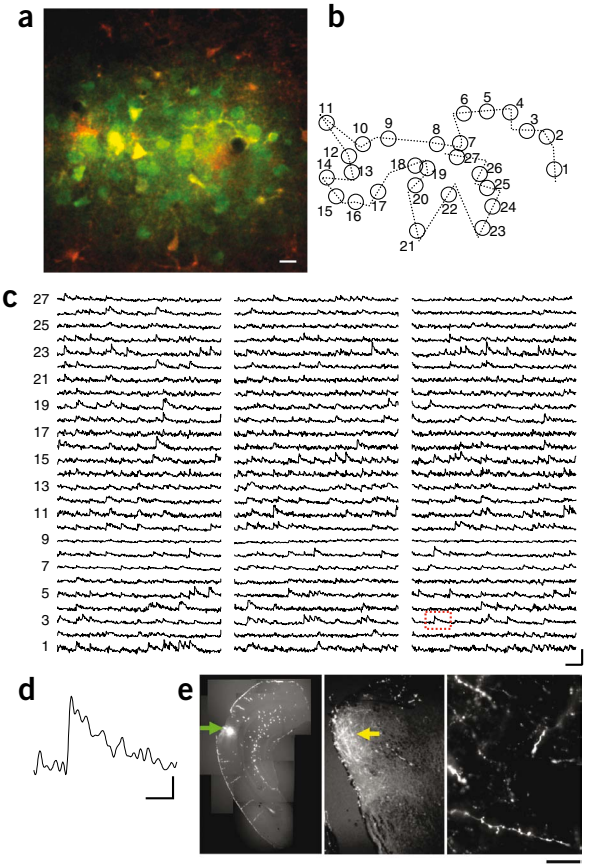

Figure 1 *In vivo* two-photon calcium imaging from dozens of neurons simultaneously in A1. (**a**) *In vivo* two-photon micrograph of a single optical plane in A1 after bolus loading of Fluo-4 a.m. (green) and SR101 (red). This optical plane is 381 µm below the pia. Scale bar represents 10 µm. (**b**) A drawing of the path of the line scan that was chosen to image 27 cells from **a**. (**c**) Relative changes in fluorescence ($\Delta F/F$) of the 27 neurons shown in **a** and **b** during presentation of a stimuli series (not shown). Scale bars represent 1 s and 50% $\Delta F/F$. (**d**) A single calcium transient enlarged from **c** (red dotted box). Scale bars represents 250 ms and 10% $\Delta F/F$. (**e**) Left, a fluorescent micrograph of a coronal slice following electroporation of dextran-rhodamine into A1 (green arrow). Middle, micrograph of a coronal slice of the medial geniculate body (MGB) from the same mouse. Labeled axons project to the ventral MGB (yellow arrow). Right, high-resolution micrograph of axonal projections in the ventral MGB shown in the middle panel. Scale bar represents 1,200 µm (left), 600 µm (middle) and 20 µm (right).

Because *in vivo* two-photon calcium imaging has not been used previously in the auditory cortex, we performed several control experiments to evaluate our optical measurements and relate them to known cellular and electrophysiological properties of neurons in A1. We first compared the optical signal coming from neurons, astrocytes and neuropil. Neurons exhibited typical calcium transients with a fast rise time (50–90 ms) and a slow exponential decay (500–1,000 ms) (**Fig. 1c**,**d**). Astrocytes showed slow fluctuations of fluorescence on the order of seconds and the neuropil showed no obvious signal (**Supplementary Fig. 2**). To further analyze the origin of the optical signal, we calculated the pixel-by-pixel correlation along the scanned line. Signals from neighboring pixels inside neuronal somata were substantially correlated, whereas there was little or no correlation between the signals from somata and their neighboring neuropil (**Supplementary Fig. 3**), confirming that our signal comes from the neurons and not from the neuropil.

We next studied the relationship between the calcium transients and spiking activity. We performed simultaneous calcium imaging and electrophysiological loose-patch recordings from labeled neurons *in vivo* using two-photon targeted patch[16] ($n = 10$ neurons from 7 mice; **Fig. 2a**). Calcium transients reliably followed spikes with high consistency (**Fig. 2b**). Single spikes induced robust calcium transients (14 ± 4.8% $\Delta F/F$). Although the exact number of spikes could not be accurately predicted from the calcium transients, double and triple spike bursts induced significantly higher $\Delta F/F$ values as compared with single spikes (23 ± 8% and 29 ± 11.5%, respectively, one-way ANOVA, $F_{2,76} = 26.6$, $P = 1.8 \times 10^{-9}$; **Fig. 2b**,**c**). Moreover, slow, nontransient increases in fluorescence were not associated with spikes. These data prompted us to develop an algorithm that identifies spike-triggered calcium

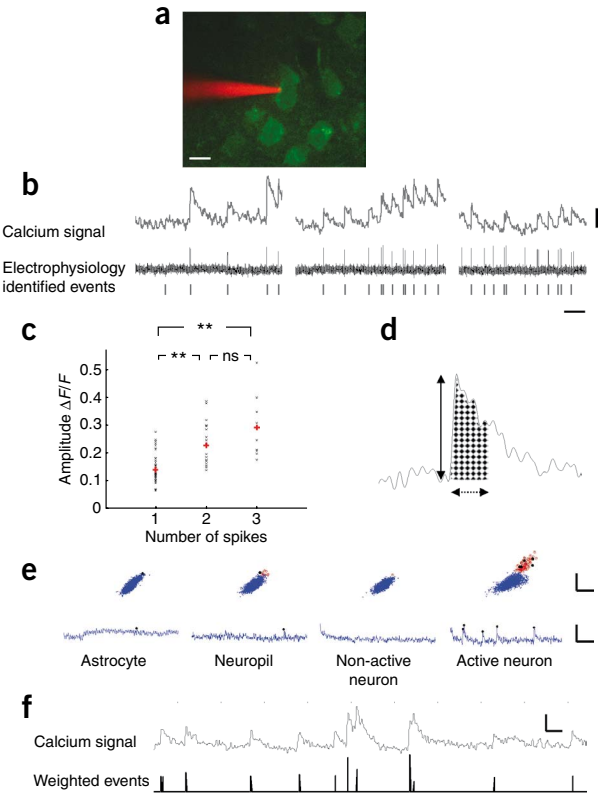

Figure 2 Identification of spike-induced calcium transients. (**a**) *In vivo* two-photon micrograph of a patch pipette loaded with Alexa 594 attached to a Fluo-4–loaded neuron. Scale bar represents 10 µm. (**b**) Simultaneous imaging and loose-patch traces of spontaneous activity *in vivo* (upper and middle traces, respectively). Bottom ticks indicate the events identified by the algorithm as being spike evoked. Scale bars represent 1 s and 20% $\Delta F/F$. (**c**) A plot of transient amplitude as a function of the number of evoking spikes ($n = 120$). Means are marked in red (paired t test, ** $P < 0.01$, ns indicates not significant, $P > 0.05$). (**d**) A single calcium transient labeled with the parameters used by the algorithm: transient amplitude (vertical line) and transient area (dashed area). (**e**) Top, distributions of transient amplitude and transient area. Scale bars represent 20% $\Delta F/F$ and 10 arbitrary units. Bottom, examples of raw calcium traces taken from the distribution above. Scale bars represent 30% $\Delta F/F$ and 2 s. Distributions and traces are shown for an astrocyte, neuropil, nonactive neuron and an active neuron. Red circles denote the events identified as being spike triggered by the algorithm. Black dots in the distribution correspond to black dots in the traces. (**f**) A representative example of a calcium signal (top) with its corresponding weighted events (bottom). Scale bars represent 20% $\Delta F/F$ and 600 ms.

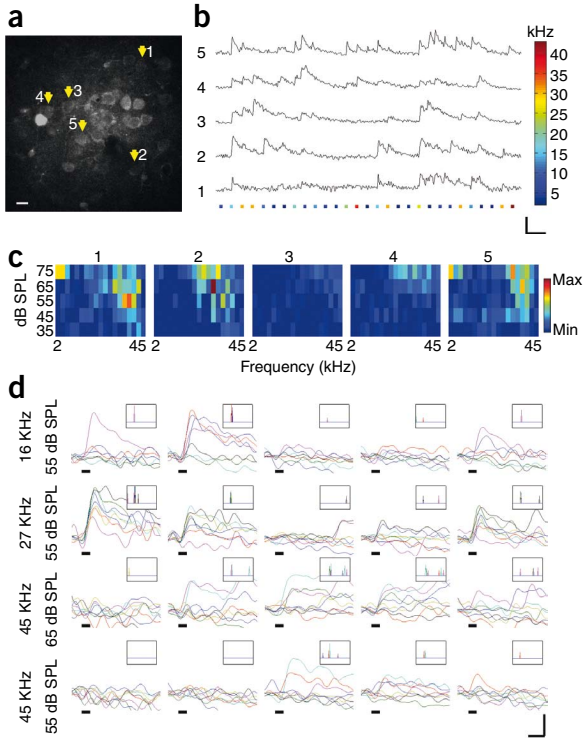

Figure 3 Single-trial and mean response profiles to pure tones. (**a**) A two-photon micrograph of Fluo-4–loaded neurons from a single optical plane. Scale bar represents 10 μm. (**b**) A 15-s representative example of relative change in fluorescence from five neurons imaged simultaneously (neurons in **a** indicated by arrows). Dots mark tone presentations. Color codes for frequency of stimulation. Scale bars represent 1 s and 30% $\Delta F/F$. (**c**) FRAs of the five neurons shown in **a** and **b**. (**d**) Single trial responses of the five neurons (same neurons as in **a**–**c**) to four different stimuli. Columns mark neurons 1–5 from left to right and rows mark different stimuli. Each panel indicates the responses to all trials of the specific stimulus. Black lines mark the stimulus. Scale bars represent 100 ms and 20% $\Delta F/F$. Insets show the weighted events that were identified by the algorithm for these traces. SPL, sound pressure level.

transients from the optical signal (**Fig. 2d**,**e**). These transients were then converted to 'weighted events', whose amplitudes are equal to the calcium transients' amplitudes. Thus, the time of an event expresses the beginning of a spiking event and the weight of an event is approximately proportional to the number of spikes that triggered it (**Fig. 2f**).

For each local peak in a trace, we computed two values: the peak amplitude and the $\Delta F/F$ area of the transient (**Fig. 2d**). Plotting these values for traces with no typical spike-related transients resulted in a roughly two-dimensional normal distribution (**Fig. 2e**). Neuronal traces containing calcium transients had a noticeable 'tail' in addition to the two-dimensional cloud. This tail corresponded with high precision to the high peaks of the calcium transients (**Fig. 2e**). The algorithm used the shape and density of the two-dimensional cloud to identify the transients in the tail, and these transients were classified as being triggered by spikes. We tested this analysis on optical traces in which we simultaneously recorded the spiking activity of the neurons. For optically well-separated neurons, 95% of the identified events were spike-triggered (that is, 5% of the events were false positives) and 91% of the spikes were successfully identified. This performance is comparable to that of recent imaging reports in other cortical areas[12,13].

In vivo, it is expected that a single optical section will cross some neurons at the center of their somata and through the periphery of others. Because the optical signal coming from the periphery of the soma was degraded compared with the signal from the center of the soma, some neurons were expected to yield weak or no transients (**Fig. 1** and **Supplementary Fig. 4**). To evaluate the quality of the signal coming from each neuron, we computed a separation score of the transients in each trace (Online Methods). Traces that had robust and clear $\Delta F/F$ transients resulted in high separation scores and vice versa. The higher the separation score, the better the performance of the algorithm in detecting spike-evoked transients (data not shown). We defined a separation threshold and all traces that did not pass it were excluded from the database. In total, we imaged 1,627 neurons in 11 animals, up to 197 putative neurons per mouse, and up to 32 neurons simultaneously. Of these neurons, 895 of 1,627 (55%) passed the separation threshold and were analyzed in detail using weighted, spike-triggered events. For clarity, we classified all neurons according to the quality of their traces and their response properties (**Supplementary Fig. 5**).

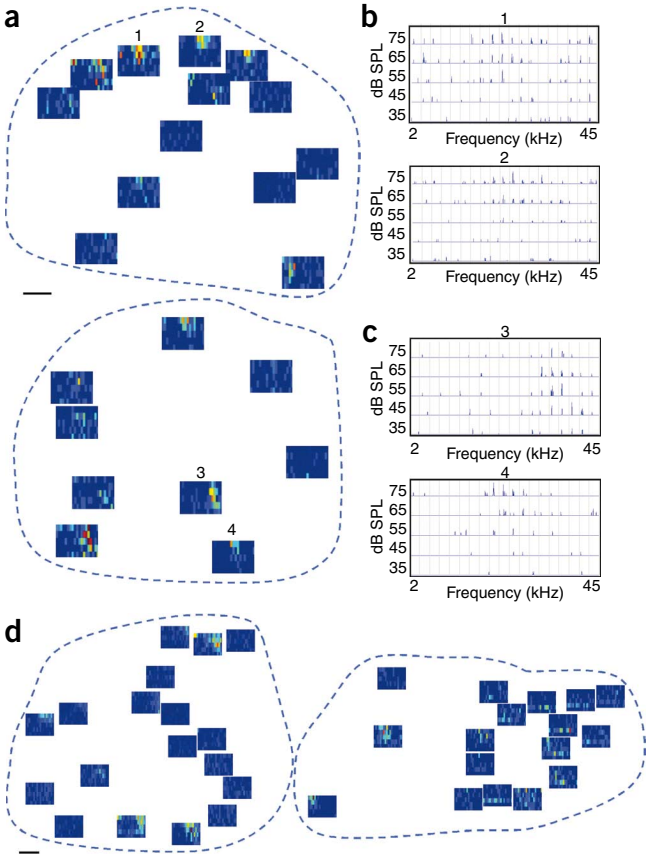

Figure 4 Functional micro-architecture in A1 is heterogeneous. (**a**) Two examples of FRA maps from different mice. Each map is constructed from a single optical plane of neurons that were imaged simultaneously. Each FRA is drawn at the location of the neuron from which it was derived. Scale bar represents 10 μm. (**b**) A post-stimulus time histogram matrix representation of two FRAs marked as 1 and 2 in **a** showing that nearby neurons can have very similar response profiles. Each cell in the matrix is the sum of all events that occurred following the presentations of the corresponding stimulus. (**c**) Data are presented as in **b** for the FRAs marked 3 and 4 in **a** showing that close by neurons can have very different response profiles. (**d**) Two additional FRA maps as in **a** from two different experiments. Scale bar represents 10 μm.

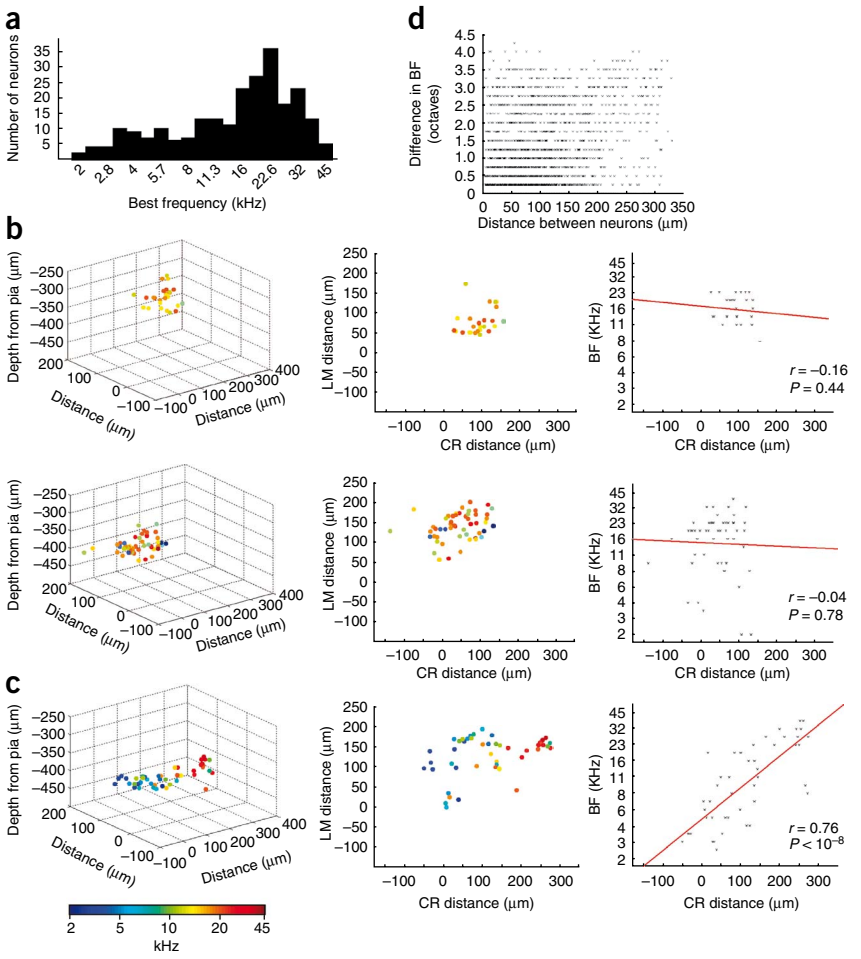

Figure 5 Local populations in A1 are not organized tonotopically. (**a**) Distribution histogram of best frequencies from all neurons in the dataset with a clear best frequency ($n = 241$ neurons). (**b**) Diagrams of neuronal locations coded by their best frequency. Rows correspond to two different experiments. Left and center panels show the positions of the neurons, color coded according to their best frequency in a side view and a top view, respectively. Right, plots of the neurons best frequencies and their relative distances along the rostro-caudal axis (CR). LM, lateral-medial. (**c**) Data are presented as in **b**, but for a mouse with two injection sites, covering a larger cortical surface. (**d**) Difference in best frequency as a function of distance between pairs of neurons, data grouped from all experiments ($n = 3,783$ pairs). Distance is measured in the two-dimensional rostro-caudal, lateral-medial plane.

Local organization in A1 is heterogeneous and sparse

To study tonal response profiles, we presented 760 pure tones at each focal plane (19 frequencies from 2–45 kHz, 5 attenuation levels, 8 repeats). We derived average responses of each neuron to the different stimuli and displayed them as frequency response areas (FRAs; **Fig. 3a–c**). Calcium responses to different stimuli were generally heterogeneous between different neurons and between different trials, although many neurons showed a consistent selectivity to some stimuli (**Fig. 3c,d**).

A recent study in marmosets proposed that heterogeneity in FRA shapes might be an important component of sound processing in awake animals[17]. Thus, we asked whether our dataset, from anesthetized mice, also reveals heterogeneity in FRA shapes. We classified all responsive neurons with nonpatchy FRAs[6,17] (comprising 267 of 895 of all imaged neurons) as either V (decreasing frequency selectivity with increasing intensity), I (narrow, level-tolerant tuning), O (nonmonotonic) or sound intensity–tuned FRAs (**Supplementary Fig. 6**). Of 267 neurons, 54% (145 of 267) had V-shaped, 11% (30 of 267) had I-shaped, 27% (71 of 267) had O-shaped and 8% (21 of 267) had intensity-tuned FRAs. Although these numbers differ from those of awake marmosets, especially in the proportion of O-shaped FRAs (27% versus 64%), this distribution is highly heterogeneous compared to previous extracellular electrophysiological studies in rodents[18,19] (but see ref. 6), suggesting that our method was not biased toward neurons with specific response patterns.

We next studied the spatial organization of neurons with respect to their FRAs. We plotted anatomical maps in which we positioned each FRA at the location of the neuron from which it was derived (**Fig. 4a**). These FRA maps revealed a variable array of different FRA shapes even in a single imaging window (~250 × 250 μm). Neighboring neurons could have very similar (**Fig. 4b**) or very different FRAs (**Fig. 4c**).

We next examined the organization of tone-responsive and unresponsive neurons. Many neurons did not show any tone-driven responses (25%, 226 of 895) or had significant tone-driven responses ($P < 0.05$), but did not show significant stimulus selectivity ($P > 0.05$, 33%, 293 of 895) (**Fig. 4a,d**). In 10 of 11 experiments, the spatial distribution of unresponsive neurons was not significantly different ($P > 0.05$) from a random distribution (see Online Methods), suggesting that unresponsive neurons do not cluster together, but are instead scattered in the local circuitry. Moreover, the precise location of a neuron in the circuit does not seem to impose strong constraints on its tone-driven response profile.

To what extent is tonotopy expressed at the level of local circuits? To answer this question, we analyzed neurons with a clear best frequency ($n = 241$ neurons). As seen previously[8], the best frequency distribution across the population was not uniform, peaking between 16–32 kHz (**Fig. 5a**). By plotting the relative position of all these neurons in each mouse, we found that there was no clear local tonotopy in 10 of 11 mice, as demonstrated by the lack of correlation between the position of a neuron along the rostro-caudal axis and its best frequency (**Fig. 5b**). In one experiment, we imaged neurons from two injection sites, thus covering a larger area. In this case, we observed a clear and significant tonotopic axis ($r = 0.76$, $P < 10^{-8}$; **Fig. 5c**). It therefore seems that tonotopy exists on large scales (>~250 μm), but breaks down at finer scales.

To quantify local heterogeneity in best frequencies across the data, we plotted the difference in best frequency as a function of the distance between neurons in all pairs with a clear best frequency ($n = 241$ neurons, 3,783 pairs from 11 mice; **Fig. 5d**). Notably, neurons located just 50–100 μm away from each other could have best frequencies that differed by up to four octaves (**Fig. 5d**). A1 in mice represents about six octaves along its full rostro-caudal axis (which is ~1 mm).

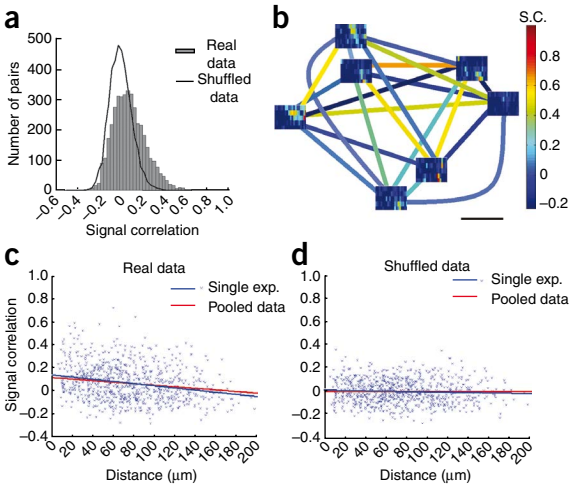

Figure 6 Signal correlations between neurons in local networks are low on average and are variable and decrease with distance. (**a**) Distribution histogram of the signal correlation values between all pairs in the dataset of simultaneously imaged neurons (gray bars) and for shuffled FRAs (black line) ($n = 3{,}926$ pairs). (**b**) Schematic presentation of signal correlation values between a representative group of neurons from one mouse in one optical plane. Each FRA is drawn at the location of the neuron from which it was derived. Color of lines between each pair of FRAs codes the signal correlation value. Scale bar represents 20 μm. SC, signal correlation. (**c**) Signal correlation values as a function of distance between neurons from a single experiment (blue dots and line, $n = 835$ pairs). Red line is the best linear fit to the data from all the pooled data ($n = 3926$ pairs, $n = 11$ mice). (**d**) Data are presented as in **c** but after randomly shuffling each FRA.

As not all frequencies are equally represented in A1 (ref. 8; **Fig. 5a**), even smooth tonotopy would predict uneven shifts in best frequencies along the cortical surface. The largest shifts in tonotopy that have been reported in large-scale mapping experiments are ~0.5–1 octaves for a distance of 100 μm[8]. Our data, showing substantially larger variability in best frequencies over such distances (up to four octaves per 100 μm and even in 50 μm), argues against smooth tonotopy and in favor of functional heterogeneity in local circuits in A1.

The best frequency of a neuron, although being an important determinant of its sensory responses, does not reflect other response properties such as intensity selectivity. To analyze functional organization on the basis of a more complete representation of the receptive fields, we calculated the signal correlation between pairs of FRAs. Signal correlation measures the degree of similarity between the average responses of pairs of neurons to all stimuli. A maximal signal correlation value of +1 implies perfectly correlated response profiles, whereas a minimum of −1 implies complementary response profiles. We calculated the signal correlation by employing a modified version of signal correlation, which removes the contribution of noise correlations (see Online Methods). As expected from the weak tonotopy, the mean signal correlation between all pairs of simultaneously measured neurons was low (0.082 ± 0.15, 3,926 pairs). Nevertheless, the rather low signal correlation values were significantly higher than those computed between shuffled FRAs (paired t test, $P < 10^{-10}$; **Fig. 6a**). The mean signal correlation values between neurons recorded nonsimultaneously from different optical planes were similarly low (0.068 ± 0.15, $n = 30{,}218$ pairs).

Although the heterogeneous FRA maps suggest a lack of a strict relationship between FRA similarity and distance (**Figs. 4** and **6b**), there was a significant (although small) decrease in signal correlation with distance ($r = -0.14$, $P < 10^{-10}$; **Fig. 6c**,**d**). Specifically, high signal correlation values were rare at larger distances, whereas both high and low signal correlation values were found at short distances. These data imply that although tonotopy breaks down at finer scales, there is nevertheless a tendency for neurons with highly similar FRAs to reside in proximity.

Local dynamics in A1

Although signal correlation quantifies the similarity between average response profiles of the neurons, the trial-by-trial tendency of neurons to fire together (or not) is not captured by this measure. We therefore calculated the noise correlation between all pairs of neurons that we imaged simultaneously. Noise correlation measures the tendency of neurons to respond together above and below their average response to the specific stimulus on individual trials[20]. Some pairs responded independently across trials, resulting in noise correlation around 0 (**Fig. 7a**), whereas others had a strong tendency to respond

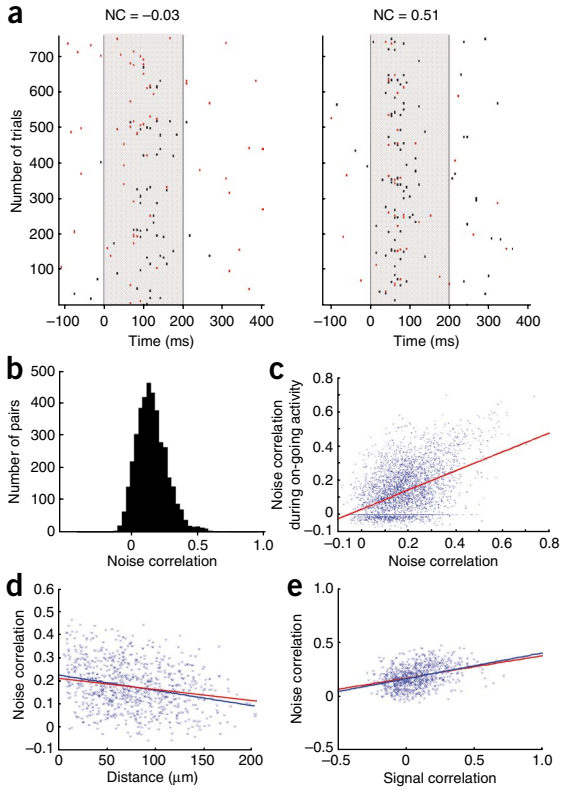

Figure 7 Noise correlations in local networks are high on average and variable and decrease with distance. (**a**) Raster plots of the calcium event responses of two pairs of neurons to all 760 stimuli. Left, a pair of neurons with low noise correlation (–0.03). Right, a pair of neurons with high noise correlation (0.51). Each row corresponds to –100 ms to +400 ms after stimulus onset. Calcium events are marked by ticks (red or black for the two neurons). Gray bars mark the time window considered a response. (**b**) Distribution histogram of noise correlation values between all simultaneously imaged neurons ($n = 3{,}926$ pairs). (**c**) A plot of noise correlation during ongoing activity as a function of noise correlation during auditory stimulation for all pairs of simultaneously imaged neurons ($n = 3{,}926$ pairs). The red line indicates the best linear fit to the data. (**d**) A plot of noise correlation as a function of distance between neurons from a single experiment (blue dots and line, $n = 835$ pairs). The red line indicates the best linear fit to the data from all the pooled data. (**e**) A plot of noise correlation as a function of signal correlation for all pairs in a single experiment (blue dots and line, $n = 835$ pairs). The red line indicates the best linear fit of all the pooled data.

in the same trials, resulting in high noise correlation (**Fig. 7a**). Over the entire population ($n = 3{,}926$ pairs), the pair-wise noise correlation values had a mean ± s.d. of 0.183 ± 0.111 (**Fig. 7b**). Notably, there was a small tail of higher values, indicating that a small number of pairs (106 of 3,926, 2.7%) had unusually high noise correlations (>0.42).

We next tested whether the neurons that we imaged simultaneously tended to be active together when not driven by stimuli. We performed the same noise correlation analysis, but in time windows immediately preceding each stimulus presentation. Noise correlations during on-going activity were lower and more variable than noise correlations during tone stimulation (mean ± s.d. of 0.133 ± 0.136). We then examined whether pairs of neurons that tended to respond together in response to tonal stimuli also tended to fire together spontaneously. We found a strong and significant correlation between the pair-wise noise correlation during tone-evoked and ongoing activity ($r = 0.46$, $P < 10^{-10}$; **Fig. 7c**).

Is the amount of noise correlation (during stimulation) between a pair of neurons related to the distance between the pair? To answer this, we plotted noise correlation values as a function of distance between neurons (**Fig. 7d**). Noise correlation decreased significantly with distance ($r = -0.17$, $P < 10^{-10}$), implying that nearby neurons have stronger tendencies to respond together than distant ones. However, at any distance, different pairs could have a wide range of noise correlation (**Fig. 7d**).

Finally, we tested whether neurons with similar FRAs also tend to respond in the same trials. This comparison revealed a significant positive correlation between the signal correlation and the noise correlation of pairs of neurons ($r = 0.275$, $P < 10^{-10}$; **Fig. 7e**). Despite this trend, there were still pairs with a high signal correlation that were not noise correlated and vice versa.

DISCUSSION

In vivo two-photon calcium imaging enabled us to characterize the functional architecture of neuronal populations in layer 2/3 of the mouse primary auditory cortex with high precision. Because neighboring cortical neurons (<100 μm apart) have a high probability of sharing common input[21,22] and being synaptically connected[21–23], one might expect that local populations of neurons would be homogeneous in their response properties. However, our data revealed a highly heterogeneous local population in which neighboring neurons could have very similar or very different response properties.

Despite the local disorder, large-scale organizing principles do exist. Tonotopy and gradual decrease of signal correlation with distance were found when examining larger distances. It thus seems that local heterogeneity is embedded in larger-scale order in A1. Furthermore, imaging dozens of neurons simultaneously allowed us to unravel temporal interactions between thousands of neuronal pairs as measured by noise correlations. Despite the heterogeneous organization with regard to signal correlation, neurons tended to have similar noise correlation during on-going and tone-driven activities, suggesting that noise correlations reflect structure in the local network (see below).

Calcium imaging of cortical circuits in A1

Sensory responses in A1 have mostly been studied with electrophysiology[9,19,24]. Unlike electrophysiology, imaging allows monitoring of the activity of dozens of precisely localized neurons simultaneously[10–13,25,26]. Furthermore, imaging is an unbiased sampling technique, relatively non-invasive, and enables coverage of hundreds of neurons in a small cortical volume. The resulting large datasets not only increase efficient data collection for experimentation, but also enable thorough sampling of local neuronal populations.

Imaging, however, measures light rather than voltage, thus reporting voltage fluctuations only indirectly. It was therefore important to calibrate our optical signal with simultaneously recorded spikes (**Fig. 2**). Only 55% of our original neurons reliably reported spikes, at least partly as a result of variability in the position of the neurons relative to the focal plane (**Supplementary Fig. 4**).

We used line scans, in contrast with the full-frame acquisition used in some previous studies[11–13]. Although line scans sample fewer pixels per neuron, they provide substantially higher sampling rates as compared with full frames (250–300 Hz versus 1–30 Hz, respectively); such rates are essential for capturing the fast rising phase of the calcium transients, whose duration is fairly short (50–90 ms) and cannot be adequately captured at sampling rates below 100 Hz. In addition, we used the indicator Fluo-4 instead of the more widely used OGB, as Fluo-4 gave rise to substantially less optical signals from the neuropil[13] (**Supplementary Figs. 2** and **3**).

We conducted our experiments under ketamine-medetomidine anesthesia. Ketamine was selected primarily because this anesthetic was used in a number of studies serving as important references for large-scale tonotpic organization in mouse A1 (refs. 8,27). In addition, ketamine-medetomidine anesthesia allows for future time-lapse experiments, which is one advantage of *in vivo* imaging[28]. Despite these advantages, anesthesia clearly has its drawbacks. Specifically, ketamine-medetomidine has been shown to increase tonal selectivity in the cat and increase response variability in rats, suggesting that tonotopy would actually appear to be more strict and regular under anesthesia[29,30]. Thus, the heterogeneity that we found might be even greater in the awake state. However, the precise effects of anesthesia on A1 neurons of mice are still not known and await evaluation, preferably on the same neurons before and during anesthesia[25].

Order and disorder in A1

Overall, our data indicate that the organization of neurons responding to pure tones in A1 is sparse and heterogeneous, as manifested by a number of measures. First, tone-responsive and selective neurons comprised only 42% of all imaged neurons (376 of 895), whereas V-shaped FRAs, which have been reported to dominate A1 (ref. 31), comprised only 16% of all imaged neurons (145 of 895). These results indicate that tone-responsive neurons are sparsely scattered in the local population in A1. Unresponsive neurons (25% of all imaged neurons) were intermingled with responsive neurons rather than being restricted to specific domains. Recently, electrophysiological experiments have shown that responsive and unresponsive neurons are located in nearby penetration sites (~50–100 μm apart) and even along a single penetration site from different cortical layers[9]. Our results support and augment these findings by showing that nonresponsive neurons are an integral part of L2/3 networks in A1 at single-cell resolution. These neurons might be involved in something other than simple pure-tone coding, such as processing of complex sound features[32].

Second, heterogeneity was evident by the wide distribution of FRA shapes. FRA diversity, and specifically O-shaped FRAs, was recently proposed to be important for auditory object recognition in awake animals[17]. Although the proportions of the different FRA types that we found were different (which may be a result of anesthesia, species specificity or cortical layer specificity), the heterogeneity of FRA shapes that we found in small volumes supports the idea that neurons with different FRA shapes may interact to process complex sounds[17]. This study focused only on responses to pure tones, whereas the local organization with regard to complex sounds awaits future investigation.

Third, heterogeneity was manifested as a lack of local organization according to best frequency (**Figs. 4** and **5**). At first, these data seem

difficult to reconcile with numerous studies showing smooth, large-scale tonotopic organization in A1 (for example, see A1 tonotopy in ferrets[19], mice[8], rats[18] and monkeys[33]). In fact, the precision of tonotopic organization in A1 has been a controversial issue for a few decades and remains unresolved to date[9,34–37].

Previous reports of smooth tonotopic maps may have resulted from techniques that average the responses over multiple neurons. Electrophysiological studies that reported precise tonotopy used electrode penetrations that were spaced by more than 200 μm and used multi-unit activity to determine frequency tuning[8,18,36,38]. Because multi-unit recordings sample spikes from neurons located at distances of up to 100 μm[39], such studies may have observed the larger-scale tonotopy while missing the local diversity of single-neuron responses. Another possible explanation for the apparent discrepancy is a sampling bias of extracellular recordings toward highly active neurons[40], raising the concern that calcium dye loading might be biased as well, penetrating preferably into subtypes of neurons with unique response profiles. Although this concern has not been thoroughly ruled out, it seems unlikely because, in at least one study, GABAergic interneuorns were loaded just as efficiently as neighboring pyramidal neurons using similar methodology[41]. Other studies revealing tonotopy using imaging techniques such as intrinsic imaging[7,42] or voltage-sensitive dyes[43] averaged responses over many neurons and are prone to overlook the local heterogeneity that we found here.

Heterogeneity was also apparent when comparing complete FRAs of all responsive neurons. The average signal correlation between all pairs of neurons was low and variable, inconsistent with the view of a highly homogeneous primary sensory cortex. In addition, local populations included neurons with highly variable FRA shapes (**Supplementary Fig. 6**).

Despite the large heterogeneity, there seems to be some order in the disorder. Nearby neurons were, on average, more similar than distant neurons. Highly correlated neurons were scarce at distances >100 μm and tonotopy was observed at distances >250 μm. Thus, the apparently different views of A1 (that is, heterogeneity versus tonotopy) may be reconciled; although rough tonotopy exists at large scales, it breaks down at fine scales (below ~250 μm), as local heterogeneity is embedded in the large-scale order. This feature may in fact be ubiquitous throughout primary sensory cortices of rodents. Studies in the visual[44] and somatosensory[12,13] cortices have shown that although global architectural features exist, neighboring neurons could have very different response properties.

It is not known whether this functional organization holds true for other species. On the one hand, there may be differences in developmental constraints between small animals such as mice, in which the whole tonotopic axis is represented in ~1 mm of cortex, and larger animals in which the tonotopic axis occupies a substantially larger area. In support of this possibility, the local organization of visual cortex may be different in rats and cats[10]. On the other hand, our data are consistent with the results of electrophysiological experiments that found high heterogeneity in neuronal response properties in A1 of both cats and rats[6,9] and low signal correlation between nearby neurons[45]. Consistently, there is evidence that tonotopy, at least in the cat, is an average characteristic[24,35].

We focused our experiments on the tonotopic organization and used pure tones. However, A1 presumably processes additional sound properties using mechanisms that are not engaged by pure tones. For example, neurons in A1 can respond in a sustained manner by their preferred stimuli, which are often more complex than pure tones[46]. Therefore, other functional organization principles that are based on other sound features (for example, organization by periodicity[47]) may well exist in A1. In this respect, imaging could serve as a powerful method for measuring response properties that go beyond pure tone coding.

Neural networks may have very different behaviors depending on the trial-by-trial correlation between neurons and may require different read-out mechanisms for the information encoded in the neural responses[1]. We found that neuronal pairs had a mean noise correlation of 0.18. Notably, this value is similar to that reported in V5 of monkeys[2,20]. Although a noise correlation of 0.18 for a given pair of neurons could be seen as rather weak, the effect on information storage of the network at these values could be marked[20,48,49]. Generally, this level of correlations would substantially limit the advantage of pooling over large populations of neurons to increase the signal-to-noise ratio of the sensory responses. This would in turn support a model in which small subgroups of neurons respond to each stimulus presentation.

Local organization in A1

Our main finding consists of highly heterogeneous local populations with relatively large correlations between a minority of neighboring neurons. What type of local connectivity might give rise to these results?

The simplest connectivity model to consider would be that of a tonotopic input combined with locally random (noisy) connectivity. This model could partially explain our results, including the heterogeneous micro-architecture and the decrease of signal and noise correlations with distance. Our data, however, put additional constraints on this connectivity model. Specifically, at short distances, a minority of the neurons are coupled rather strongly, whereas such coupling is absent at longer distances. These findings are consistent with the random connectivity model provided that there is at least one component of the overall connectivity that is strong, sparse and decreases fast with distance. Such a model would result in the formation of small subnetworks of highly correlated neurons, partially overlapping in space.

A number of our findings support such a subnetworks model. Notably, a subnetworks model would account for the details of the dependence of signal correlation and noise correlation on distance. Specifically, at short distances we observed both very large and very small correlations, while at longer distances we observed only smaller correlations. In consequence, the scatter of correlations and distances had a wedge shape for both signal and noise correlations. In contrast, a smooth gradient model would presumably result in a constant variance with distance. In the subnetworks model, there are pairs belonging to both the same and to different subnetworks at short distances (resulting in high and low correlations, respectively, and overall in high variability), whereas only pairs from different subnetworks would be found at long distances. In support of this argument, we performed a set of computer simulations to compare our signal correlation versus distance data to different organizational layouts and found that it was most consistent with a subnetworks model (see **Supplementary Discussion** and **Supplementary Fig. 7**). In addition, the strong correlation between the signal correlation of pairs of neurons (generally attributed to common input), and the noise correlation between them (generally attributed to direct synaptic connections) supports a model of strongly coupled subnetworks that share common input. Such a model, with partially overlapping, strongly connected subnetworks that share common input, has already been suggested for L2/3 neurons in the visual cortex[50]. Finally, our data describing strong correlation between noise correlation during on-going activity and during auditory stimuli support the idea that distributed groups of interconnected neurons are coactivated during tone stimulation.

Although our data seems to best fit the overlapping subnetworks model, it is only one interpretation of our results. Different experimental procedures, including direct mappings of synaptic

connectivity in local cortical circuits, would be required to reveal the underlying organizational principles of the auditory cortex.

METHODS

Methods and any associated references are available in the online version of the paper at http://www.nature.com/natureneuroscience/.

Note: Supplementary information is available on the Nature Neuroscience website.

ACKNOWLEDGMENTS

We thank H. Sompolinsky and E. Zohary for critically commenting on early versions of this manuscript. We thank N. Taaseh and A. Yaron-Jakoubovitch for their kind technical assistance during the early stages of this project. We thank Y. Rubin and J. Schiller for the software module of the line scan. We thank J. Linden for her help on cortical recordings in mice. We thank all the members of the Mizrahi laboratory and A. Eban-Rothschild for their helpful comments and discussions. This work was supported in part by a grant from Citizens United for Research in Epilepsy and by a European Research Council grant to A.M. (#203994), and by a grant of the European Union FP6 to I.N. (NOVELTUNE consortium).

AUTHOR CONTRIBUTIONS

G.R., I.N. and A.M. designed the experiments together and wrote the paper together. G.R. performed the experiments and analyzed the data.

COMPETING INTERESTS STATEMENT

The authors declare no competing financial interests.

Published online at http://www.nature.com/natureneuroscience/.
Reprints and permissions information is available online at http://www.nature.com/reprintsandpermissions/.

1. Averbeck, B.B., Latham, P.E. & Pouget, A. Neural correlations, population coding and computation. *Nat. Rev. Neurosci.* **7**, 358–366 (2006).
2. Cohen, M.R. & Newsome, W.T. Context-dependent changes in functional circuitry in visual area MT. *Neuron* **60**, 162–173 (2008).
3. Houweling, A.R. & Brecht, M. Behavioural report of single neuron stimulation in somatosensory cortex. *Nature* **451**, 65–68 (2008).
4. Bizley, J.K., Nodal, F.R., Nelken, I. & King, A.J. Functional organization of ferret auditory cortex. *Cereb. Cortex* **15**, 1637–1653 (2005).
5. DeWeese, M.R., Wehr, M. & Zador, A.M. Binary spiking in auditory cortex. *J. Neurosci.* **23**, 7940–7949 (2003).
6. Moshitch, D., Las, L., Ulanovsky, N., Bar-Yosef, O. & Nelken, I. Responses of neurons in primary auditory cortex (A1) to pure tones in the halothane-anesthetized cat. *J. Neurophysiol.* **95**, 3756–3769 (2006).
7. Nelken, I. *et al.* Large-scale organization of ferret auditory cortex revealed using continuous acquisition of intrinsic optical signals. *J. Neurophysiol.* **92**, 2574–2588 (2004).
8. Stiebler, I., Neulist, R., Fichtel, I. & Ehret, G. The auditory cortex of the house mouse: left-right differences, tonotopic organization and quantitative analysis of frequency representation. *J. Comp. Physiol. [A]* **181**, 559–571 (1997).
9. Hromádka, T., Deweese, M.R. & Zador, A.M. Sparse representation of sounds in the unanesthetized auditory cortex. *PLoS Biol.* **6**, e16 (2008).
10. Ohki, K., Chung, S., Ch'ng, Y.H., Kara, P. & Reid, R.C. Functional imaging with cellular resolution reveals precise micro-architecture in visual cortex. *Nature* **433**, 597–603 (2005).
11. Ohki, K. *et al.* Highly ordered arrangement of single neurons in orientation pinwheels. *Nature* **442**, 925–928 (2006).
12. Kerr, J.N. *et al.* Spatial organization of neuronal population responses in layer 2/3 of rat barrel cortex. *J. Neurosci.* **27**, 13316–13328 (2007).
13. Sato, T.R., Gray, N.W., Mainen, Z.F. & Svoboda, K. The functional microarchitecture of the mouse barrel cortex. *PLoS Biol.* **5**, e189 (2007).
14. Stosiek, C., Garaschuk, O., Holthoff, K. & Konnerth, A. *In vivo* two-photon calcium imaging of neuronal networks. *Proc. Natl. Acad. Sci. USA* **100**, 7319–7324 (2003).
15. Llano, D.A. & Sherman, S.M. Evidence for nonreciprocal organization of the mouse auditory thalamocortical-corticothalamic projection systems. *J. Comp. Neurol.* **507**, 1209–1227 (2008).
16. Komai, S., Denk, W., Osten, P., Brecht, M. & Margrie, T.W. Two-photon targeted patching (TPTP) *in vivo*. *Nat. Protoc.* **1**, 647–652 (2006).
17. Sadagopan, S. & Wang, X. Level invariant representation of sounds by populations of neurons in primary auditory cortex. *J. Neurosci.* **28**, 3415–3426 (2008).
18. Kilgard, M.P. & Merzenich, M.M. Distributed representation of spectral and temporal information in rat primary auditory cortex. *Hear. Res.* **134**, 16–28 (1999).
19. Sally, S.L. & Kelly, J.B. Organization of auditory cortex in the albino rat: sound frequency. *J. Neurophysiol.* **59**, 1627–1638 (1988).
20. Zohary, E., Shadlen, M.N. & Newsome, W.T. Correlated neuronal discharge rate and its implications for psychophysical performance. *Nature* **370**, 140–143 (1994).
21. Holmgren, C., Harkany, T., Svennenfors, B. & Zilberter, Y. Pyramidal cell communication within local networks in layer 2/3 of rat neocortex. *J. Physiol. (Lond.)* **551**, 139–153 (2003).
22. Thomson, A.M., West, D.C., Wang, Y. & Bannister, A.P. Synaptic connections and small circuits involving excitatory and inhibitory neurons in layers 2–5 of adult rat and cat neocortex: triple intracellular recordings and biocytin labeling *in vitro*. *Cereb. Cortex* **12**, 936–953 (2002).
23. Song, S., Sjostrom, P.J., Reigl, M., Nelson, S. & Chklovskii, D.B. Highly nonrandom features of synaptic connectivity in local cortical circuits. *PLoS Biol.* **3**, e68 (2005).
24. Abeles, M. & Goldstein, M.H. Jr. Functional architecture in cat primary auditory cortex: columnar organization and organization according to depth. *J. Neurophysiol.* **33**, 172–187 (1970).
25. Greenberg, D.S., Houweling, A.R. & Kerr, J.N. Population imaging of ongoing neuronal activity in the visual cortex of awake rats. *Nat. Neurosci.* **11**, 749–751 (2008).
26. Kerr, J.N., Greenberg, D. & Helmchen, F. Imaging input and output of neocortical networks *in vivo*. *Proc. Natl. Acad. Sci. USA* **102**, 14063–14068 (2005).
27. Linden, J.F., Liu, R.C., Sahani, M., Schreiner, C.E. & Merzenich, M.M. Spectrotemporal structure of receptive fields in areas AI and AAF of mouse auditory cortex. *J. Neurophysiol.* **90**, 2660–2675 (2003).
28. Wallace, D.J. *et al.* Single-spike detection *in vitro* and *in vivo* with a genetic Ca2+ sensor. *Nat. Methods* **5**, 797–804 (2008).
29. Kisley, M.A. & Gerstein, G.L. Trial-to-trial variability and state-dependent modulation of auditory-evoked responses in cortex. *J. Neurosci.* **19**, 10451–10460 (1999).
30. Zurita, P., Villa, A.E., de Ribaupierre, Y., de Ribaupierre, F. & Rouiller, E.M. Changes of single unit activity in the cat's auditory thalamus and cortex associated to different anesthetic conditions. *Neurosci. Res.* **19**, 303–316 (1994).
31. Recanzone, G.H., Guard, D.C. & Phan, M.L. Frequency and intensity response properties of single neurons in the auditory cortex of the behaving macaque monkey. *J. Neurophysiol.* **83**, 2315–2331 (2000).
32. Sadagopan, S. & Wang, X. Nonlinear spectrotemporal interactions underlying selectivity for complex sounds in auditory cortex. *J. Neurosci.* **29**, 11192–11202 (2009).
33. Philibert, B. *et al.* Functional organization and hemispheric comparison of primary auditory cortex in the common marmoset (*Callithrix jacchus*). *J. Comp. Neurol.* **487**, 391–406 (2005).
34. Evans, E.F., Ross, H.F. & Whitfield, I.C. The spatial distribution of unit characteristic frequency in the primary auditory cortex of the cat. *J. Physiol. (Lond.)* **179**, 238–247 (1965).
35. Goldstein, M.H. Jr., Abeles, M., Daly, R.L. & McIntosh, J. Functional architecture in cat primary auditory cortex: tonotopic organization. *J. Neurophysiol.* **33**, 188–197 (1970).
36. Merzenich, M.M. Knight, P.L. & Roth, G.L. Representation of cochlea within primary auditory cortex in the cat. *J. Neurophysiol.* **38**, 231–249 (1975).
37. Schreiner, C.E. & Sutter, M.L. Topography of excitatory bandwidth in cat primary auditory cortex: single-neuron versus multiple-neuron recordings. *J. Neurophysiol.* **68**, 1487–1502 (1992).
38. Reale, R.A. & Imig, T.J. Tonotopic organization in auditory cortex of the cat. *J. Comp. Neurol.* **192**, 265–291 (1980).
39. Henze, D.A. *et al.* Intracellular features predicted by extracellular recordings in the hippocampus *in vivo*. *J. Neurophysiol.* **84**, 390–400 (2000).
40. Margrie, T.W., Brecht, M. & Sakmann, B. *In vivo*, low-resistance, whole-cell recordings from neurons in the anaesthetized and awake mammalian brain. *Pflugers Arch.* **444**, 491–498 (2002).
41. Sohya, K., Kameyama, K., Yanagawa, Y., Obata, K. & Tsumoto, T. GABAergic neurons are less selective to stimulus orientation than excitatory neurons in layer II/III of visual cortex, as revealed by *in vivo* functional Ca2+ imaging in transgenic mice. *J. Neurosci.* **27**, 2145–2149 (2007).
42. Mrsic-Flogel, T.D., Versnel, H. & King, A.J. Development of contralateral and ipsilateral frequency representations in ferret primary auditory cortex. *Eur. J. Neurosci.* **23**, 780–792 (2006).
43. Chakraborty, S., Sandberg, A. & Greenfield, S.A. Differential dynamics of transient neuronal assemblies in visual compared to auditory cortex. *Exp. Brain Res.* **182**, 491–498 (2007).
44. Mrsic-Flogel, T.D. *et al.* Homeostatic regulation of eye-specific responses in visual cortex during ocular dominance plasticity. *Neuron* **54**, 961–972 (2007).
45. Chechik, G. *et al.* Reduction of information redundancy in the ascending auditory pathway. *Neuron* **51**, 359–368 (2006).
46. Wang, X., Lu, T., Snider, R.K. & Liang, L. Sustained firing in auditory cortex evoked by preferred stimuli. *Nature* **435**, 341–346 (2005).
47. Schulze, H. & Langner, G. Periodicity coding in the primary auditory cortex of the Mongolian gerbil (*Meriones unguiculatus*): two different coding strategies for pitch and rhythm? *J. Comp. Physiol. [A]* **181**, 651–663 (1997).
48. Schneidman, E., Berry, M.J. II, Segev, R. & Bialek, W. Weak pair-wise correlations imply strongly correlated network states in a neural population. *Nature* **440**, 1007–1012 (2006).
49. Sompolinsky, H., Yoon, H., Kang, K. & Shamir, M. Population coding in neuronal systems with correlated noise. *Phys. Rev. E* **64**, 051904 (2001).
50. Yoshimura, Y., Dantzker, J.L. & Callaway, E.M. Excitatory cortical neurons form fine-scale functional networks. *Nature* **433**, 868–873 (2005).

ONLINE METHODS

Animal preparation. We used male and female NMRI mice (total of $n = 28$ mice, 8–12-weeks-old), anesthetized using ketamine (100 mg per kg of body weight) and medetomidine (0.83 mg per kg). Depth of anesthesia was assessed by monitoring the pinch withdrawal reflex. Dextrose-saline was injected subcutaneously to prevent dehydration. Body temperature was maintained at 36–38 °C. The skull was exposed, cleaned and dried. A metal pin was glued to the skull and attached to a custom-made head holder allowing precise orientation of the head relative to the objective. The muscle overlying the left auditory cortex was removed and a craniotomy (~3 × 3 mm) was performed. The dura was gently removed and the cortical surface was kept continuously moist. Following each experiment, animals were killed by overdose with sodium pentobarbital. All experiments were approved by the Hebrew University Animal Care and Use Committee.

Dye loading and two-photon imaging. The auditory cortex was loaded with Fluo-4 a.m. (F14201, Invitrogen) using multicell bolus loading[14]. Fluo-4 a.m. was dissolved in 20% Pluronic F-127 in DMSO (vol/vol, P-6867, Invitrogen) to a concentration of 10 mM and further diluted tenfold in external buffer containing 125 mM NaCl, 5 mM KCl, 10 mM glucose, 10 mM HEPES, 2 mM $CaCl_2$, 2 mM $MgSO_4$ and 0.1 mM sulforhodamine 101.

Injections were performed under visual guidance using two-photon excitation. The solution was slowly injected into the cortex (duration 1–3 min) using a quartz pipette into a diameter of ~250 µm per injection. In one experiment, two injections were made in a distance of a few hundred microns. The craniotomy was sealed with a thin layer of 2.5% agarose (wt/vol, type IIIa, Sigma-Aldrich), glass coverslipped and secured with dental cement. The mouse was placed under the microscope and the cranial window was oriented perpendicular to the objective lens.

Imaging was carried out on an Ultima microscope (Prairie Technologies) with a 40× (0.8 NA) IR–Achroplan water-immersion objective (Olympus). A femtosecond laser (Mai-Tai Spectra Physics) was used to excite Fluo-4 at 800 nm. Line-scan images were acquired at 200–300 Hz, depending on the length of the line. Lines were acquired at consecutive series of 2,000–5,000 lines with an inter-series interval of ~1.4 s. The line-scan software was developed and kindly provided to us by Y. Rubin and J. Schiller (Technion). Neurons were imaged at depths of 250–450 µm under the pia, corresponding to layers 2/3 of the cortex. Imaging was stable with no movements caused by heartbeat or respiration. Neurons with distinctly high basal fluorescence typically showed weak or no fluorescence transients (presumably because they were close to saturation). Imaging started 30 min post injection and lasted for ~3 h. Scan timings, stimuli delivery and electrophysiological recordings were acquired using a standard data acquisition board (Digidata 1440A, Molecular Devices) on a separate PC.

The experiments were conducted in an isolated room and in complete silence. Background noise (coming especially from the laser chiller and galvo scanners) consisted mostly of frequencies below 2 kHz, and averaged $-10\frac{\text{dB}}{\sqrt{\text{Hz}}}$ in the range of presented frequencies (2–45 kHz).

Loose-patch recordings from Fluo-4–loaded neurons. Fluo-4–loaded neurons were recorded in a loose-patch configuration ($n = 10$ neurons from 7 mice). Quartz pipettes (tip resistance 7–9 MΩ) contained 140 mM potassium gluconate, 4 mM NaCl, 0.5 mM $CaCl_2$, 5 mM Mg-ATP, 5 mM EGTA, 10 mM HEPES and 0.05 mM Alexa 594 (pH = 7.2). Fluo-4–loaded neurons were targeted using two-photon targeted patch[16]. Unlike the imaging-only experiments, the craniotomy was not sealed with glass, but only covered with agarose. Spikes were recorded using an intracellular amplifier in current clamp mode (Multiclamp 700B, Molecular Devices) and acquired at 10 kHz (Digidata 1440A, Molecular Devices). Calcium imaging was performed simultaneously as described above.

Auditory stimulation. Auditory stimuli were generated online using custom-written software (Matlab) through an electrostatic loudspeaker driver and a programmable attenuator (ED1, PA5, Tucker Davis Technologies). The loudspeaker (ES1) was placed ~10 cm from the right ear of the mouse. Acoustic stimuli consisted of a series of randomly presented pure tones at 19 frequencies ranging from 2–45 kHz and at five to six attenuation levels ranging from 35–75 dB SPL. Each combination of frequency attenuation was presented eight times. Tone duration was 50 ms, including 5-ms ON and OFF linear ramps, with a 400-ms inter-stimulus interval.

Histology. We labeled cortico-thalamic projections ($n = 6$ mice) by electroporation of dextran-rhodamine into the same location as the imaging experiments, as described previously[15]. To verify the cortical layer of imaging, we combined targeted electroporation with immunolabeling ($n = 4$ mice) using the primary antibody SMI-32 (ab28029, Abcam, 1:1,000) and CY5-conjugated goat antibody to mouse as a secondary antibody (1:400, 115-175-003, Jackson Immunoresearch Laboratories). Images were acquired on a fluorescent microscope (Olympus IX70), processed off-line using ImageJ or Matlab and adjusted for brightness and contrast.

Data analysis. Statistical tests are considered to be significant at the 0.05 level. All data is presented as mean ± s.d. Low-pass filtering of all $\Delta F/F$ traces was performed using a finite impulse response filter designed by the Matlab function fir1. The duration of the impulse response was 50 ms and the cutoff frequency was the sampling frequency divided by 10. To keep the temporal features of the calcium signal in their correct locations, we used the function filtfilt to achieve zero-phase filtering, effectively corresponding to two passes of the low-pass filter.

To study the relationship between the calcium transients and spikes, we used the simultaneous imaging and electrophysiological experiments from which we developed an algorithm to automatically identify spike-evoked calcium transients as follows. For each local peak in a trace, we computed the transient peak amplitude, calculated as $\Delta F/F_{\text{peak}} - \Delta F/F_{\text{peak}-100\text{ ms}}$, and the transient area, calculated as $\int_{\text{peak}-100}^{\text{peak}+500} \Delta F/F$. Plotting these two values for traces with no clear transients (for example, noise, astrocytes and nonactive neurons) resulted in a roughly normally distributed cloud of points. In contrast, plotting these values for neurons with clear transients resulted in an additional tail of points extending to higher values outside the two-dimensional cloud. This tail corresponded with good accuracy to the peaks of the calcium transients. Tails were automatically identified by the algorithm on the basis of the high density of the points in the cloud (corresponding to many local maxima in the trace) and its oval shape. Points in the tail were assigned as spike-evoked transients. In addition, transients that occurred during the decaying part of a previous transient were detected and also assigned as spike evoked.

Each distribution was assigned a separation score that was calculated by summing the squared distances of all points in the tail from the center of the cloud, divided by the overall number of peaks. This score expresses the quality of the separation between the calcium transients and the noisy $\Delta F/F$ fluctuations.

The algorithm was trained on ~30% of the loose-patch and simultaneous imaging data and tested on the rest. As expected, a higher separation score indicated that the algorithm was better able to detect spikes. To limit our analyses to traces with reliable spike-evoked activity, we set a separation threshold (75 arbitrary units) such that only traces on which the algorithm detected spikes from transients with >95% accuracy passed this threshold. This single threshold (75 arbitrary units) was then used as criteria for the test set in the combined experiments data and for all neurons in the entire dataset. All neurons that passed this threshold were considered as having well-separated traces. Calcium traces that did not pass this separation threshold were eliminated from further analysis. Finally, the analog $\Delta F/F$ traces were converted to discrete events by applying the algorithm's criteria described above. Events were assigned a weight equal to the transient's amplitude and all further analyses were performed on these weighted events.

By converting the fluorescence traces to weighted events, some information in the fluorescence trace is lost. For example, slow drifts in baseline fluorescence were not converted to events. Such drifts may report some physiological processes that are not tightly correlated with spikes. We focused only on calcium changes that could be used as a proxy for spiking activity. We did not pursue any physiological roles of calcium in A1 neurons that were not associated with spikes.

FRAs were constructed from the 95 average responses to all of the unique frequency-attenuation combinations. Individual responses were calculated as

the sum of all events in a 10–200-ms time window following stimulus onset. The best frequencies of the FRAs were determined manually, but were chosen blind to the specific experiment from which the FRA originated. If a best frequency could not be clearly determined, the neuron was classified as not having a clear best frequency. All FRAs in each imaging session were color-scaled to the maximal and minimal pixel values for all FRAs in the session. FRA shapes were classified manually according to the following criteria. FRAs showing decreasing frequency selectivity with increasing intensity were classified as being V shaped, constant frequency selectivity with increasing intensity was classified as being I shaped, responsiveness to a small range of intensities and frequencies was classified as being O shaped if the peak response was not to the highest intensity, and high selectivity to 1–2 intensity levels with no clear selectivity for frequency was classified as being intensity tuned.

To estimate whether a neuron was responsive to pure tones, we compared its responses during the 200 ms just preceding and just following stimulus onset using a paired *t* test ($P < 0.05$). This is a conservative test given that many stimuli did not elicit a response, but were nevertheless included in the test. Response selectivity of a neuron was tested using a one-way ANOVA on the 95 stimuli, with the single-trial responses as repetitions.

To test whether unresponsive neurons were spatially clustered, we calculated the sum of the distances between all unresponsive pairs. We then calculated distances between the same number of random neurons in the imaging volume and plotted this distribution for 1,000 runs. In 10 of 11 experiments, the distance between the unresponsive neurons was not in the lowest 5% of the distances between randomly chosen neurons, indicating that unresponsive neurons were not significantly clustered.

Signal correlations were, roughly speaking, the correlation coefficients between the FRAs. However, as a result of the small number of repeats of each individual stimulus, noise correlations could significantly bias the signal correlations. Therefore, a correction procedure was required. The single-trial responses of a neuron were estimated as above by the sum of the weighted events in the 10–200-ms time window following stimulus onset. Each cell had 760 single-trial responses to 95 stimuli (19 frequencies, 5 attenuations and 8 repeats). The correlation between the FRAs of two neurons (i and j) is the correlation between their responses to all stimuli.

$$R(c_i,c_j) \equiv \frac{\mathrm{cov}(c_i,c_j)}{\sqrt{\mathrm{cov}(c_i,c_i)\times \mathrm{cov}(c_j,c_j)}}$$

$$\mathrm{cov}(c_i,c_j) \equiv E_S[(c_i(s) - <c_i>_s)\times(c_j(s) - <c_j>_s)] =$$

$$\frac{1}{\#s}\sum_S (c_i(s) - <c_i>_s)\times(c_j(s) - <c_j>_s)$$

where c_i are the responses of cell i, $c_i(s)$ are the responses of cell i to stimulus s and $<c_i>_s$ is the mean response of cell i over all stimuli.

However, we do not have the exact responses $c_i(s)$, only their estimates based on a finite number of trials. We therefore estimated $c_i(s)$ by their averages over all trials in which stimulus s was presented. As a result, the elements in the last product can be written in terms of the single-trial responses $c_i(s,r)$

$$(c_i(s) - <c_i>_s) = \frac{1}{\#r}\sum_r (c_i(s,r) - <c_i>_s)$$

$$(c_j(s) - <c_j>_s) = \frac{1}{\#r}\sum_r (c_j(s,r) - <c_j>_s)$$

The product becomes

$$(c_i(s) - <c_i>_s)\times(c_j(s) - <c_j>_s) =$$

$$\frac{1}{\#r^2}\sum_r\sum_{r'}(c_i(s,r) - <c_i>_s)\times(c_j(s,r') - <c_j>_s)$$

The expected value of the terms in this expression, where the expectation is taken over the trials and stimuli, is equal to the covariance of the average responses provided that $r \neq r'$. If $r = r'$, the expected value of the product would include a contribution resulting from noise correlations. In our case, the noise correlation was typically higher than the signal correlation, and it may contribute substantially to the estimates of the signal correlations. To avoid errors in the estimates of signal correlation by noise correlation contamination, we then removed these terms from the sum. Thus, we estimated the contribution of stimulus s to the covariance.

$$\frac{1}{\#r^2 - r}[\sum_r\sum_{r'}(c_i(s,r) - <c_i>_s)\times(c_j(s,r') - <c_j>_s) -$$

$$\sum_{r''}(c_i(s,r'') - <c_i>_s)\times(c_j(s,r'') - <c_j>_s)$$

If we denote the last expression as *corrected_product*, then

$$\mathrm{cov}_{\mathrm{corrected}}(c_i,c_j) = \frac{1}{\#s}\sum_s corrected\_product$$

and the correlation coefficient becomes

$$R_{\mathrm{corrected}}(c_i,c_j) = \frac{\mathrm{cov}_{\mathrm{corrected}}(c_i,c_j)}{\sqrt{\mathrm{cov}_{\mathrm{corrected}}(c_i,c_i)\times \mathrm{cov}_{\mathrm{corrected}}(c_j,c_j)}}$$

The correlations between the fluctuations of the single-trial responses of pairs of neurons around their mean response were used as the pair-wise noise correlations. From each single-trial response of a neuron, we subtracted the mean response of the neuron to that stimulus. For each neuron, this resulted in a vector of fluctuations around the mean responses to the different stimuli. The noise correlation was the correlation coefficient between these vectors.

doi:10.1038/nn.2484